PAPER

Check for updates

Self-powered solar-blind ultraviolet-visible Cu₂O/Ga₂O₃ photodetectors†

Xiaodan Wang,[ab] Jianping Xu, (ID) ⋆[a] Shaobo Shi,[c] Lina Kong,[b] Xiangwei He,[a] Jiahang He,[a] Xiaosong Zhang (ID) [b] and Lan Li⋆[b]

Traditional optical communication using single narrow-band photodetectors (PDs) has poor confidentiality because all information and data are exposed to free space. With the development of science and technology, even the optical communication in the solar-blind ultraviolet (UV) band carries the risk of eavesdropping. Dual-band PDs have potential applications in secure and reliable optical communication through a combination of optical encryption and algorithmic encryption. In this paper, self-powered Cu₂O/Ga₂O₃ heterojunction PDs with solar-blind UV-visible photodetection were fabricated. By adjusting the pH value of the Cu₂O electrolyte, the crystallization quality and grain orientation of the Cu₂O thin film were improved, and the interface transfer resistance of the heterojunctions was decreased. The Cu₂O/Ga₂O₃ PDs fabricated in Cu₂O electrolyte with a pH value of 9.5 demonstrated the optimized solar-blind UV-visible photoresponse characteristics. In the absence of applied bias, the device exhibited a responsivity of 0.12 mA W⁻¹, a rise time of 2.48 ms and a fall time of 11.72 ms at 254 nm. The responsivity reaches 19 mA W⁻¹ when illuminated at 475 nm, and the rise and fall times are 0.96 and 9.12 ms, respectively. Utilizing the excellent photoresponse characteristics of the solar-blind UV-visible band, the device was used to design and demonstrate a proof-of-concept optical communication system for secure data transmission. The proposed system features two independent light channels, utilizing solar-blind UV light as the information carrier and visible light for key transmission. By implementing specific algorithms, this design ensures safe and reliable communication.

1. Introduction

Single narrow-band photodetectors (PDs) cannot meet the requirements of high-precision target detection and information recognition. The dual-band and multi-band PDs can utilize the difference of photoresponse characteristics in the bands to realize mutual verification and mutual compensation of information, and then improve the accuracy, precision and safety of data. Among the dual-band PDs including visible-near-infrared,[1–3] UV-near-infrared,[4,5] blue-red,[6] near-infrared-short infrared,[7] and UV-visible,[8–10] UV-visible dual-band PDs are widely used in flame detection, memory storage and secure communication.[11–16] Compared with the combination of multi-band PDs and line-array multi-band PDs, the PDs that achieve dual-band or even multi-band detection through a single device have the advantages of simple structure and reduced interference. The earliest multi-band single PDs were fabricated using quantum well materials utilizing the sub-band transition formed in the conduction band of doped quantum wells. Devices such as two-color PDs with a GaAlAs/GaAs quantum well structure have advantages such as flexible wavelength control and a simple preparation method.[17] The emerging heterojunction PDs constructed using semiconductors with light absorption in different wavelength bands can realize dual-band or multi-band detection. For example, Wang *et al.* fabricated PDs based on MoS₂/Si heterojunctions demonstrating a photoresponse band from the visible to infrared region.[18] He *et al.* constructed the UV-infrared PDs based on β-Ga₂O₃/BP heterojunctions.[5]

The direct ultra-wide bandgap Ga₂O₃ semiconductor material has a large optical absorption coefficient in the solar-blind UV band, good thermal stability and high breakdown voltage resistance, making it one of the preferred materials for solar-blind UV detectors.[19–21] A Ga₂O₃ thin film is generally polycrystalline. Many grain boundaries in Ga₂O₃ have a strong

a Tianjin Key Laboratory of Quantum Optics and Intelligent Photonics, School of Science, Tianjin University of Technology, Tianjin 300384, China. E-mail: xjp0335@163.com

b School of Materials Science and Engineering, Key Laboratory of Display Materials and Photoelectric Devices, Ministry of Education, and Tianjin Key Laboratory for Photoelectric Materials and Devices, Tianjin University of Technology, Tianjin 300384, China. E-mail: lilan2000us@126.com

c School of Science, Tianjin University of Technology and Education, Tianjin 300222, China

† Electronic supplementary information (ESI) available. See DOI: https://doi.org/10.1039/d4tc00965g

scattering and blocking effect on carrier transport, resulting in the decrease of photocurrent and responsivity of Ga_2O_3 PDs. Some strategies have been proposed to solve this problem from the perspectives of the crystalline quality and the control of crystal plane orientation of Ga_2O_3. Some studies have reported an improvement in the device performance by preparing ordered Ga_2O_3 nanostructures. The ordered nanorod arrays (NRs) can serve as trapping structures to enhance the light absorption, form interfaces for the separation of photogenerated charge carriers, and provide directional paths to promote carrier transmission.[22–25] In order to achieve the photoresponse characteristics in the solar-blind UV-visible band for Ga_2O_3 based PDs, Ga_2O_3 is usually compounded with a semiconductor with strong visible light absorption to construct heterojunction PDs, such as Ga_2O_3/Au/MAPbBr$_3$ sandwich structure PDs[26] and Ga_2O_3/CuSCN core–shell structure PDs.[11] Due to a strong absorption in the visible region, simple preparation and easy control of the crystal phase, Cu_2O is suitable to construct the visible light PDs. The composite of Cu_2O and Ga_2O_3 can produce heterojunction PDs with photoresponse characteristics in the solar-blind UV-visible band.

The light absorption coefficient and carriers transport capability of Cu_2O films are closely related to crystallization and grain orientation, which are key factors that determine the photoelectric characteristics of the device.[27] The electrochemical deposition conditions such as the electrolyte substances, concentration and pH value, deposition temperature, time, and current density or voltage can affect the morphology and crystallization of Cu_2O films. Herein, Cu_2O thin films were electrochemical deposited on Ga_2O_3 NRs. The morphology and crystal plane orientation of Cu_2O crystals was regulated by controlling the pH value of the electrolyte. The self-powered photoresponse characteristics of Cu_2O/Ga_2O_3 heterojunction PDs in the solar-blind UV-visible band were investigated. The self-powered photoresponse characteristics have been elaborated based on the interface contact and optoelectronic properties of Cu_2O/Ga_2O_3 heterojunctions. The PDs have been designed and demonstrated a proof-of-concept optical encryption communication system for secure data transmission utilizing the solar-blind UV light as an information carrier and visible light for key transmission.

2. Results and discussion

2.1 Morphology, crystal structure and optical properties of Cu_2O/Ga_2O_3 heterojunctions

Fig. 1 shows SEM images of Ga_2O_3 and Cu_2O films deposited on Ga_2O_3 with electrolyte solution of different pH values. As can be seen from Fig. 1(a), Ga_2O_3 nanorods grow vertically on the FTO substrate with diamond-shaped end faces, a long diagonal length of 100–200 nm and an average length of about 660 nm. The diamond shaped end face is not detected after Cu_2O deposition, and pyramid shaped Cu_2O particles form a continuous and dense film.[28] EDS results of top view and profile view in Fig. S1 (ESI†) suggested that the elements Ga,
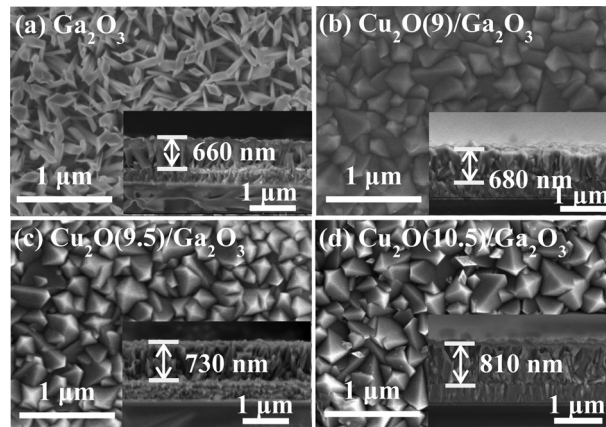

Fig. 1 The top-view and cross-sectional view of SEM images of (a) Ga_2O_3 NRs and (b) $Cu_2O(9)$/Ga_2O_3, (c) $Cu_2O(9.5)$/Ga_2O_3 and (d) $Cu_2O(10.5)$/Ga_2O_3.

O and Cu are uniformly distributed throughout the film, indicating that Cu_2O grows on the top and side walls of Ga_2O_3 nanorods. With the increase of electrolyte pH of Cu_2O, the pyramid-shaped particles of Cu_2O thin films are transformed from tetrahedron to trihedron. $Cu_2O(9)$ and $Cu_2O(9.5)$ thin films are quadrangular pyramids, and the distribution of the particle size becomes more uniform with the increased pH value, whereas the particles of $Cu_2O(10)$ film demonstrate tetrahedral and trihedral pyramid shapes. The pH value of the deposition solution can affect the growth rate of Cu_2O crystals on different crystalline surfaces, and then affects the orientation of the crystal structure of the film and the particle shapes. The oxygen atom density of the Cu_2O (111) crystalline surface is greater than that of the (200) crystalline surface. The electrolytes with smaller pH provide fewer oxygen atoms, which facilitates the rapid growth of the (200) crystalline surface with tetrahedral pyramid shapes. With the increase of the electrolyte pH value, the growth rate of the (111) crystalline surface with higher oxygen atom density gradually exceeds that of the (200) crystalline surface.[29] Therefore, particles of the $Cu_2O(10)$ film show trihedral pyramid shapes and tetrahedral pyramid shapes. The SEM profiles demonstrate that the thickness of the Cu_2O/Ga_2O_3 film increases with the increase of the electrolytic pH of Cu_2O. The thickness of the Ga_2O_3 nanorod film is about 660 nm, and that of the Cu_2O/Ga_2O_3 film is 680, 730 and 810 nm for $Cu_2O(9)$/Ga_2O_3, $Cu_2O(9.5)$/Ga_2O_3 and $Cu_2O(10.5)$/Ga_2O_3, respectively. Increase of electrolytic pH of Cu_2O is favorable to accelerate the deposition of Cu_2O particles.

Fig. 2(a) shows XRD spectra of Ga_2O_3 and Cu_2O films deposited on Ga_2O_3 with different pH electrolyte solutions. In the XRD patterns of Ga_2O_3, the stronger diffraction peak at 36° is attributed to the α-Ga_2O_3 (110) crystal plane of corundum-type structure. No peaks of the other phase were found except for the diffraction peaks originated from the FTO substrate.[30] After the electrochemical deposition of Cu_2O thin films on Ga_2O_3 substrate, Ga_2O_3 retains a corundum-type structure and presents a (110) crystal plane diffraction peak. The (110), (111), (200) and (311) crystal plane diffraction peaks
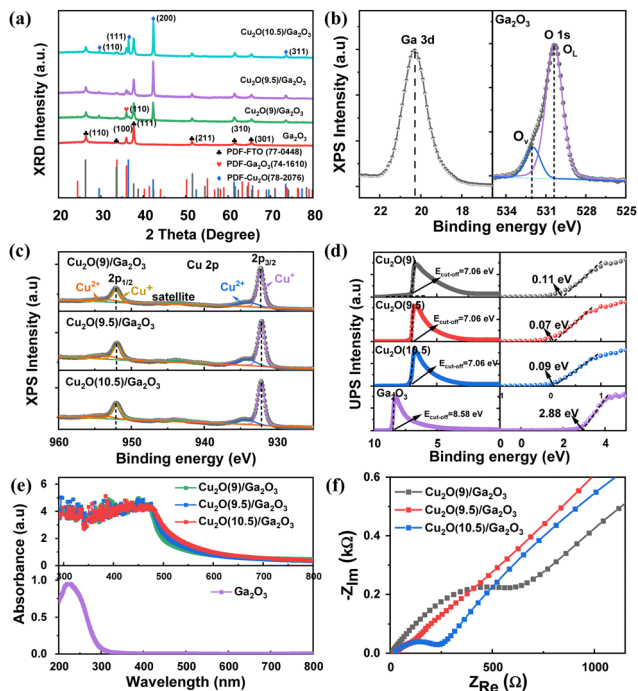
This journal is © The Royal Society of Chemistry 2024

J. Mater. Chem. C, 2024, **12**, 8944–8951 | **8945**

Fig. 2 (a) XRD patterns for Cu_2O/Ga_2O_3 with Cu_2O prepared at different pH values. (b) XPS spectra of O 1s and Ga 3d for Ga_2O_3. (c) XPS spectra of Cu 2p for Cu_2O prepared at different pH values. (d) VB spectra and UPS spectra for Ga_2O_3 and Cu_2O prepared at different pH values. (e) UV-vis absorption spectra for Ga_2O_3 and Cu_2O/Ga_2O_3 with Cu_2O prepared at different pH values. (f) EIS curves for Cu_2O/Ga_2O_3 with Cu_2O prepared at different pH values.

of Cu_2O were observed at 29.6°, 36.5°, 42.4° and 73.6°, while no other phases of Cu and Cu_xO were found.[31,32] With the increase of Cu_2O electrolyte pH, the crystal diffraction intensity of the main diffraction peak (200) of Cu_2O increases, and the (111) crystal diffraction peak of $Cu_2O(10)$ is significantly enhanced compared to the other films, which correlates with the trihedral pyramidal shapes of Cu_2O particles.

The valence states of the elements in Ga_2O_3 and Cu_2O/Ga_2O_3 were analysed using XPS spectroscopy. Fig. 2(b) shows the XPS spectra of Ga 3d and O 1s of Ga_2O_3, and the Ga 3d peak corresponds to a binding energy of 20 eV, which is consistent with the results reported in the literature.[33] The peak shape of O1s is asymmetric and can be fitted to two peaks at 530.4 (O_L) and 531.9 eV (O_V), where O_L is related to oxygen ions in the lattice and O_V is related to oxygen vacancies.[34,35] Fig. 2(c) shows the XPS spectra of Cu 2p for Cu_2O films deposited on Ga_2O_3 substrates with different pH electrolytes. Upon fitting, the peaks related to Cu $2p_{3/2}$ and Cu $2p_{1/2}$ of Cu^+ appeared at the binding energies of 932.4 and 952.3 eV, and peaks related to Cu^{2+} appeared at 934.5 and 954.7 eV, which is due to the oxidation of Cu_2O films in air.[36] Combined with the Auger spectrum of Cu in Fig. S2 (ESI†), Cu mainly exists in the form of Cu^+ in Cu_2O films.

The band structure of Ga_2O_3 and Cu_2O electrons was analyzed by using UPS valence band (VB) spectra of Fig. 2(d). Through the linear extrapolation of the cut-off edge of the Au

standard sample in the low energy region, it is calculated that the Fermi level (E_F) is −7.96 eV under the bias of −10 V. The E_F values of Ga_2O_3 and Cu_2O are calculated using the semiconductor work function formula $\Phi = (E_{cut\text{-}off} - E_F) - 21.22$, in which the cutoff energy ($E_{cut\text{-}off}$) can be linearly extrapolated from the cutoff edge of the high energy region. The $E_{cut\text{-}off}$ for Ga_2O_3 and Cu_2O are −8.58 and −7.06 eV, respectively. The calculated E_F are −4.69 and −6.2 eV for Ga_2O_3 and Cu_2O, respectively. The energy difference between the E_F and the valence band maximum (VBM) of Ga_2O_3 and Cu_2O can be analyzed by the intersection of the tangent line at the maximum of the slope and the line along the outer edge of the baseline, which are 2.88, 0.11, 0.07 and 0.09 eV for Ga_2O_3, $Cu_2O(9)$, $Cu_2O(9.5)$ and $Cu_2O(10)$, respectively. Combining the optical band gap energies of Ga_2O_3 (4.61 eV) and Cu_2O (2.07 eV) calculated from diffuse reflectance spectroscopy (Fig. S4, ESI†), the position of E_F relative to vacuum energy levels can be obtained. The E_F position of Ga_2O_3 is far from the VBM, indicating that Ga_2O_3 is an n-type semiconductor, whereas the E_F position of Cu_2O is close to the VBM, suggesting that Cu_2O is a p-type semiconductor. The UV-vis absorption spectra of Fig. 2(e) shows that Ga_2O_3 has a strong optical absorption in the deep UV region less than 250 nm, and the absorption edge is broadened to about 298 nm, which is related to the deep-level oxygen vacancy defect in Ga_2O_3.[37,38] Cu_2O/Ga_2O_3 has strong optical absorption from the solar-blind UV to the blue light region, indicating that the composite material can be used for solar-blind UV-visible light detection.

Electrochemical impedance spectroscopy (EIS) can reflect the characteristics of charge transfer at the interface of semiconductor materials. The EIS curves of Cu_2O/Ga_2O_3 tested at open-circuit voltage and frequency in the range of 0.1–10^6 Hz are given in Fig. 2(f). The radius of the semicircle in the Nyquist plot is related to the interfacial charge transfer process.[39] The size of the radius of the semicircle located in the low-frequency region is related to the charge transfer between Cu_2O and the electrolyte, and the radius of the semicircle located in the high-frequency region is related to the charge transfer at the Cu_2O/Ga_2O_3 heterojunction interface. With the increase of Cu_2O electrolyte pH, the radius of the Cu_2O/Ga_2O_3 heterojunction semicircle firstly decreases and then increases, indicating the interfacial transfer resistance of $Cu_2O(9.5)/Ga_2O_3$ is the smallest, which is favorable for the transfer of photogenerated carriers.

2.2 Self-powered photoresponse characteristics of Cu_2O/Ga_2O_3 heterojunction PDs

Fig. 3(a) shows a schematic diagram of the PD structure of Cu_2O/Ga_2O_3 PDs, where Cu_2O particles are distributed on the top and sidewalls of Ga_2O_3 nanorod arrays, and FTO and Au are used as the bottom and top electrodes, respectively. Fig. 3(b)–(d) and Fig. S5 (ESI†) show the I–V curves of Cu_2O/Ga_2O_3 heterojunction PDs prepared by Cu_2O electrolyte with different pH in the dark state, solar-blind UV light 254, 265 525, 550 and 660 nm illuminations. All PDs show obvious photosensitive characteristics and have photovoltaic effect under solar-blind
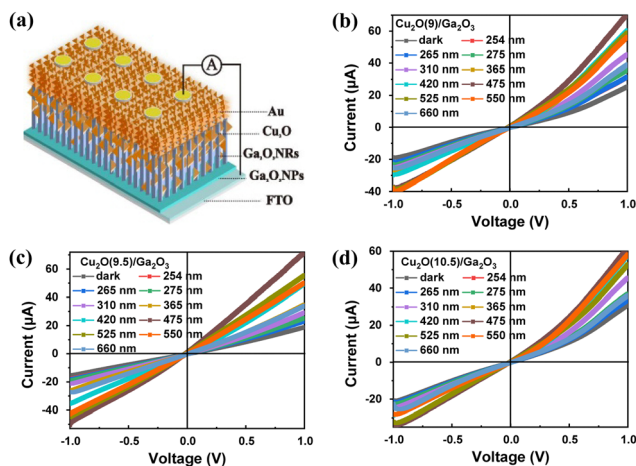
8946 | *J. Mater. Chem. C*, 2024, **12**, 8944–8951

This journal is © The Royal Society of Chemistry 2024

Fig. 3 (a) Schematic diagram of the PD structure of Cu_2O/Ga_2O_3 PDs. Dark-state and different wavelengths light illuminations $I-V$ curves for (b) $Cu_2O(9)/Ga_2O_3$ PDs, (c) $Cu_2O(9.5)/Ga_2O_3$ PDs and (d) $Cu_2O(10.5)/Ga_2O_3$ PDs under an optical power density of 4 mW cm^{-2} illumination.

UV, UV and visible illuminations, indicating that the PD can realize photodetection in the solar-blind UV-visible region under the condition of self-driving without an external electric field.

Fig. 4 shows the $I-t$ curves of the Cu_2O/Ga_2O_3 heterojunction PDs under monochromatic light from solar-blind UV to visible range without external bias. All PDs can demonstrate the self-powered photoresponse in solar-blind UV-visible region with good repeatability and stability under the light switching. The
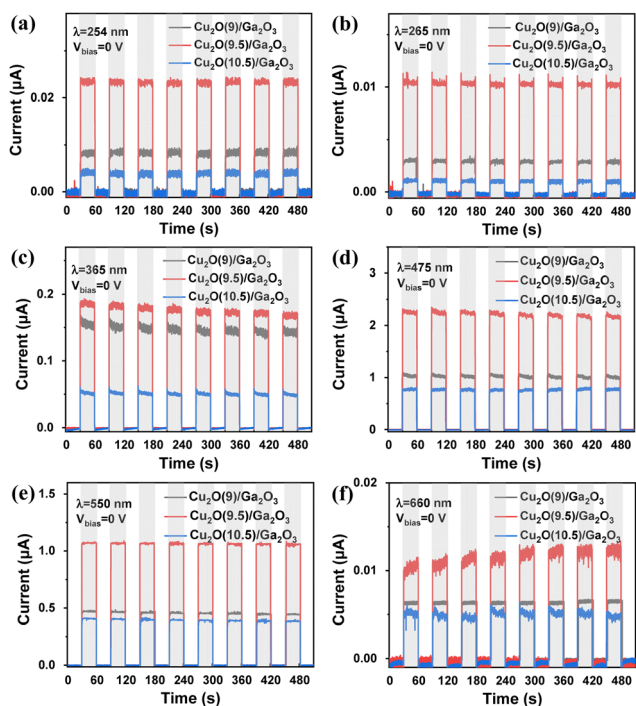

Fig. 4 $I-t$ cycling curves at zero bias for Cu_2O/Ga_2O_3 heterojunction PDs with Cu_2O at different pH values under (a) 254, (b) 265, (c) 365, (d) 475, (e) 550 and (f) 660 nm illuminations with P = 4 mW cm^{-2}.

largest photocurrent is obtained under 475 nm light for all the PDs. The $Cu_2O(9.5)/Ga_2O_3$ PD exhibits an optimized photocurrent under the monochromatic light irradiation compared to other PDs. As revealed from the absorption spectra of Cu_2O/Ga_2O_3 heterojunctions, the photocurrent of the PD in the solar-blind UV band is mainly contributed by photogenerated carriers in Ga_2O_3 NRs, and that in UV and visible bands is mainly originated from the photogenerated carriers in Cu_2O films. The photoresponse time is an important parameter to evaluate the performance of PDs. Fig. S7 (ESI†) shows the photoresponse time of heterojunction PDs with different pH values of Cu_2O electrolyte solution under 254 and 475 nm illuminations. The photoresponse time of the PDs is in the order of millisecond. The rise time τ_{rise} under illumination is shorter than the decay time τ_{decay} of photocurrent after the light is turned off. The τ_{rise} and τ_{decay} of $Cu_2O(9.5)/Ga_2O_3$ PD are the shortest and the photoresponse speed is the fastest. Table S1 (ESI†) lists the comparison of the photoresponse time of our $Cu_2O(9.5)/Ga_2O_3$ PD and other Ga_2O_3 based PDs. The Cu_2O/Ga_2O_3 PD in this work shows a relatively fast photoresponse time.

Fig. 5(a)–(d) shows the responsivity (R), detectivity (D^*), sensitivity (S) and linear dynamic range (LDR) of all PDs under different illumination wavelengths from the solar-blind UV to visible range under self-powered conditions. The PDs have
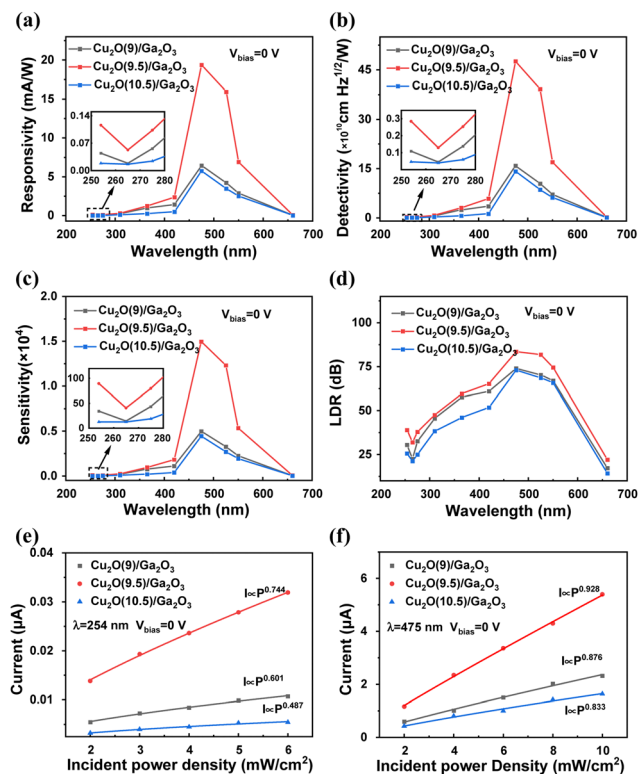
Fig. 5 Performance parameters of (a) R, (b) D^*, (c) S and (d) LDR of Cu_2O/Ga_2O_3 heterojunction PDs with Cu_2O prepared at different pH values at 0 V bias voltage under solar-blind UV, UV and visible light illuminations with 4 mW cm^{-2} optical power density. Photocurrent under (e) 254 and (f) 475 nm illuminations of Cu_2O/Ga_2O_3 heterojunction PDs at different optical power densities.

This journal is © The Royal Society of Chemistry 2024

J. Mater. Chem. C, 2024, **12**, 8944–8951 | **8947**

photoresponse characteristics in the illumination range of 254–660 nm. The parameters of the PDs firstly increase and then decrease with the increase of light wavelength, reaching the optimal values at 475 nm. The LDR of Cu_2O/Ga_2O_3 heterojunction PDs is greater than 3 dB in both UV and visible light, which can meet the commercial standard for optical communication.

Fig. 5(e) and (f) show the curves of the relationship between photocurrent and optical power density of Cu_2O/Ga_2O_3 heterojunction PDs under solar-blind UV 254 nm and visible 475 nm illumination without applied voltage, respectively. The photocurrent of the heterojunction PDs increases with increasing light density, and the heterojunction produce more photogenerated carriers when illuminated by incident light of high optical power density. The nonlinear relationship between the photocurrent (I_P) of a PD and the optical power density (P) can be expressed by a power function $I_P = AP^\theta$. A is a constant at a specific wavelength, and θ is related to the kinetic processes of photogenerated carriers including photogenerated carrier production, separation, capture, and complexation. Usually $0 < \theta < 1$, the closer the θ value is to 1, the more the photogenerated carriers contribute to the photocurrent.[40] The $Cu_2O(9.5)/Ga_2O_3$ PD derives the highest θ values, which are 0.744 and 0.928 at 254 and 475 nm, respectively. The θ values of the Cu_2O/Ga_2O_3 heterojunction PDs during visible light irradiation are larger than those under solar-blind UV illuminations, indicating higher photoelectric conversion efficiency for the heterojunction under the visible light illuminations.[41–49]

To further analyse the relationship between the self-powered photoresponse characteristics of the PDs and the energy band structure of the heterojunction, the information of the energy band structure based on the XPS, UPS and diffuse reflectance spectroscopy measurements are shown in Fig. 6. Considering that the Fermi level position of Ga_2O_3 is higher than that of Cu_2O, the energy band of Ga_2O_3 bends upwards and that of Cu_2O bends downwards at the interface after the both

semiconductors come into contact and reach thermal equilibrium, forming a barrier region of Ga_2O_3 electrons at the interface. When illuminated at 254 nm, the electrons on the valence band of Ga_2O_3 and Cu_2O are excited to the conduction band. The excited electrons in Ga_2O_3 need to tunnel through the interface barrier to Cu_2O conduction band with the lower energy, and finally are collected by Au electrode. The holes in Cu_2O are transferred to the Ga_2O_3 and then *via* Ga_2O_3 to FTO electrode. Considering 254 nm light illumination through Ga_2O_3 to Cu_2O, few photogenerated carriers can be produced in Cu_2O. The photocurrent of PDs under solar-blind UV light is mainly contributed by the photogenerated carriers of Ga_2O_3. When irradiated at 475 nm, Ga_2O_3 acts as a heterojunction window, and photogenerated carriers in Cu_2O contribute to the photocurrent of PDs. Due to the existence of a heterojunction interface barrier, photogenerated electrons of Cu_2O are collected by the Au electrode, and photogenerated holes are transferred to the FTO electrode through Ga_2O_3.

Compared with the traditional optical communication system, UV light communication has the unique advantages of high flexibility, low eavesdropping, omni-directional and non-line-of-sight communication, high reliability and good confidentiality, which has wide application prospects in the communication field. With the rapid development of optical communication, there is still a risk of information interception due to the exposure of information data in free space, which poses higher requirements for information security transmission. A proof-of-concept solar-blind UV-visible encrypted communication system is designed based on Cu_2O/Ga_2O_3 heterojunction PDs with the solar-blind UV-visible photoresponse characteristics. The PD can be used as a receiving terminal to decode the information as a binary "1" state for a photocurrent value greater than 0.5 μA and a binary "0" state for a value less than 0.5 μA. Solar-blind UV light is used as a carrier to transmit the encrypted message A, and visible light as a carrier to transmit the key message B with the same number of binary bits. The encryption agreement is defined as follows: when the binary bit in B is "0", the information corresponding to that of A ("0" or "1") is false, and its inverse code ("1" or "0") is output. On the other hand, when the binary bit in B is "1", the information corresponding to that of A ("0" or "1") is true, and the original code ("0" or "1") is output. For example, the solar-blind UV light transmits the encrypted message A as "11011000", the visible light transmits the same number of binary bit key message B as "01110000", and the real message decoded by the encryption agreement is "01010111". The
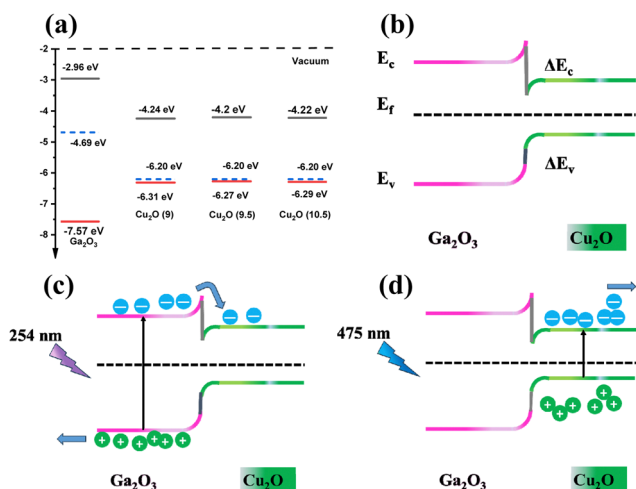
Fig. 6 Energy band structures of Ga_2O_3 and Cu_2O prepared at different pH values (a) before and (b) contact. The schematic diagram of carrier transport of Cu_2O/Ga_2O_3 heterojunction under (c) 254 (d) 475 nm illuminations.
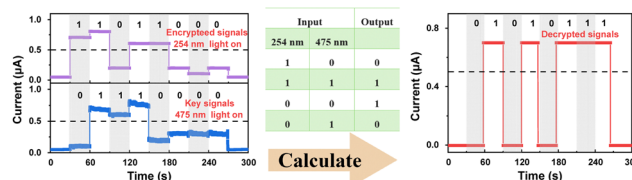

Fig. 7 Schematic diagram of the calculation process of secure optical communication.

8948 | *J. Mater. Chem. C*, 2024, **12**, 8944–8951

This journal is © The Royal Society of Chemistry 2024

schematic diagram of the calculation process of secure optical communication is shown in Fig. 7. Only PDs with solar-blind UV-visible band photoresponse and agreed-upon encryption algorithms can obtain real information, indicating significant potential for application in safety communication within the realm of secure and efficient data transmission.

3. Experimental

3.1 Preparation of Ga_2O_3 NRs

The Ga_2O_3 NRs were grown on the seed layer by using a hydrothermal method. Firstly, the Ga_2O_3 seed layers were prepared by using a sol–gel method on FTO substrates using the precursor solution obtained from 0.3086 g of gallium nitrate hydrate (Aladdin, $\geq$99%), 12 mL of ethylene glycol methyl ether (Aladdin, $\geq$99.3%), and 72 μL of ethanolamine (Aladdin, $\geq$99.5%) stirred in a water bath at 60 °C for 1 h. The as-grown films were annealed for 1 h at 500 °C in air. Secondly, Ga_2O_3 seed layers were placed in the growth solution of 0.03 M $Ga(NO_3)_3 \cdot xH_2O$, 0.005 M $C_6H_{12}N_4$ and 30 mL DI water, and kept for 6 h at 150 °C. Finally, Ga_2O_3 NRs were obtained by annealing at 500 °C in air for 4 h.

3.2 Preparation of Cu_2O/Ga_2O_3

Cu_2O thin films were prepared on Ga_2O_3 NRs by electrochemical deposition in the solution with different pH values. Firstly, 10 g $CuSO_4 \cdot 5H_2O$ (Aladdin, 85–90%) was dissolved in a certain amount of DI water and stirred for 30 min, then 22.4 mL lactic acid was added, and then an appropriate amount of DI water was added to 100 mL. The stirring was continued for 30 min, and the pH value of the solution was adjusted to 9, 9.5 and 10.5 with NaOH to obtain deposition electrolytes. Cu_2O thin films were electrochemically deposited at 60 °C in a three-electrode system using Ga_2O_3 NRs as the working electrode, platinum plated titanium mesh as the counter electrode and Ag/AgCl as the reference electrode. The deposition current was 6 mA and the deposition time was 10 min. According to the different pH values of electrolytes, Cu_2O/Ga_2O_3 samples were named $Cu_2O(9)/Ga_2O_3$, $Cu_2O(9.5)/Ga_2O_3$ and $Cu_2O(10.5)/Ga_2O_3$. Finally, Au electrodes were sputtered on the heterojunction films to construct PDs.

3.3 Characterization and measurements

The surface morphology of the samples was characterized via field emission scanning electron microscopy (SEM, Hitachi S-8010). The crystal structure was studied via X-ray diffractometry (XRD, Rigaku D/max 2500/PC). The elemental composition and chemical state were analyzed through X-ray electron spectroscopy (XPS, Thermo ESCALAB-250), in which the photon energy of the monochromatic source (Al target) was 1846 eV. The band structure of the samples was tested by using He–I ($h\nu$ = 21.22 eV) UV photoelectron spectroscopy (UPS). The absorption and diffuse reflectance spectra of Cu_2O thin films and Ga_2O_3 NRs were measured using a Hitachi V4100 and a Shimadzu UV-3600i Plus UV-visible spectrophotometer, respectively. Electrochemical impedance spectroscopy (EIS) data were obtained in

1 M Na_2SO_4 solution with an electrochemical workstation (Autolab PGSTAT 128N) using a three-electrode system with the sample as the working electrode, a platinum wire as the counter electrode, and Ag/AgCl as the reference electrode. The current–voltage (I–V) and current–time (I–t) curves in darkness and illumination were measured using a Keithley 2450 source meter and a light emitting diode (LED). The photoresponse time was obtained using an oscilloscope (Tektronix MDO3014).

4. Conclusions

In summary, Cu_2O/Ga_2O_3 heterojunction PDs with a self-powered solar-blind UV-visible photoresponse have been constructed. By adjusting the pH value of the Cu_2O electrolyte, the crystallization quality and grain orientation of $Cu_2O(9.5)$ films were improved, and the interface transfer resistance of $Cu_2O(9.5)/Ga_2O_3$ heterojunction was reduced. The optimized solar-blind UV-visible photoresponse characteristics without the external bias were achieved in $Cu_2O(9.5)/Ga_2O_3$ PDs, demonstrating a responsivity of 0.12 mA W^{-1}, rise/decay time of 2.48/11.72 ms under 254 nm illumination, and responsivity of 19 mA W^{-1}, the rise/decay time of 0.96/9.12 ms under 475 nm illumination. A secure solar-blind UV-visible optical communication system with two independent optical channels is proposed by using the photoresponse characteristics of solar-blind UV-visible band PDs, in which solar-blind UV is used as the information carrier and visible light as the key. Information can be transmitted through an encryption algorithm via secure and reliable communication. This method has a good application prospects in the field of secure communication.

Author contributions

Xiaodan Wang: conceptualization, data curation, formal analysis, writing – original draft. Jianping Xu: conceptualization, formal analysis, resources, funding acquisition. Shaobo Shi: formal analysis. Lina Kong: formal analysis. Xiangwei He: formal analysis. Jiahang He: formal analysis. Xiaosong Zhang: formal analysis. Lan Li: formal analysis, resources, project administration, supervision.

Conflicts of interest

The authors declare that they have no known competing financial interests or personal relationships that could have appeared to influence the work reported in this paper.

This journal is © The Royal Society of Chemistry 2024

J. Mater. Chem. C, 2024, 12, 8944–8951 | 8949

References

1 M. Dai, H. Chen, R. Feng, W. Feng, Y. Hu, H. Yang, G. Liu, X. Chen, J. Zhang, C.-Y. Xu and P. Hu, A Dual-Band Multi-layer InSe Self-Powered Photodetector with High Performance Induced by Surface Plasmon Resonance and Asymmetric Schottky Junction, *ACS Nano*, 2018, **12**, 8739–8747.

2 P. Wang, S. Liu, W. Luo, H. Fang, F. Gong, N. Guo, Z. G. Chen, J. Zou, Y. Huang, X. Zhou, J. Wang, X. Chen, W. Lu, F. Xiu and W. Hu, Arrayed van der Waals Broadband Detectors for Dual-Band Detection, *Adv. Mater.*, 2017, **29**, 1604439.

3 Y. Gao, C. Zhao, K. Pu, M. He, W. Cai, M.-C. Tang, F. Kang, H.-L. Yip and G. Wei, Low-voltage-modulated Perovskite/organic Dual-band Photodetectors for Visible and Near-infrared Imaging, *Sci. Bull.*, 2022, **67**, 1982–1990.

4 S. Chen, C. Teng, M. Zhang, Y. Li, D. Xie and G. Shi, A Flexible UV-Vis-NIR Photodetector based on a Perovskite/Conjugated-Polymer Composite, *Adv. Mater.*, 2016, **28**, 5969–5974.

5 T. He, C. Li, X. Zhang, Y. Ma, X. Cao, X. Shi, C. Sun, J. Li, L. Song, C. Zeng, K. Zhang, X. Zhang and B. Zhang, Metalorganic Chemical Vapor Deposition Heteroepitaxial β-Ga_2O_3 and Black Phosphorus Pn Heterojunction for Solar-Blind Ultraviolet and Infrared Dual-Band Photodetector, *Phys. Status Solidi A*, 2019, **217**, 1900861.

6 B. Huang, J. Liu, Z. Han, Y. Gu, D. Yu, X. Xu and Y. Zou, High-Performance Perovskite Dual-Band Photodetectors for Potential Applications in Visible Light Communication, *ACS Appl. Mater. Interfaces*, 2020, **12**, 48765–48772.

7 C. h Xu, S. H. Luo, Y. Wang, X. F. Shi, C. Fu, J. Wang, C. Y. Wu and L. B. Luo, Bias-Selectable Si Nanowires/PbS Nanocrystalline Film n–n Heterojunction for NIR/SWIR Dual-Band Photodetection, *Adv. Funct. Mater.*, 2023, **33**, 2214996.

8 F. Cao, Z. Q. Li, X. Y. Liu, Z. F. Shi and X. S. Fang, Air Induced Formation of CsBiBr/CsBiBr Bulk Heterojunction and Its Dual-band Photodetection Abilities for Light Communication, *Adv. Funct. Mater.*, 2022, **32**, 2206151.

9 M.-M. Fan, K.-L. Xu, X.-Y. Li, G.-H. He and L. Cao, Self-powered Solar-blind UV/visible Dual-band Photodetection based on a Solid-state PEDOT:PSS/α-Ga_2O_3 Nanorod Array/FTO Photodetector, *J. Mater. Chem. C*, 2021, **9**, 16459–16467.

10 T. T. Yan, Z. Q. Li, L. Su, L. M. Wu and X. S. Fang, Bidirectional and Dual-Mode Organic Photodetector Enables Secure Ultraviolet Communication, *Adv. Funct. Mater.*, 2023, **33**, 2302746.

11 S. Li, D. Guo, P. Li, X. Wang, Y. Wang, Z. Yan, Z. Liu, Y. Zhi, Y. Huang, Z. Wu and W. Tang, Superhigh Signal-to-Noise Ratio, Self-Powered Solar-blind Photodetector Based on n-Ga2O3/p-CuSCN Core–Shell Microwire Heterojunction, *ACS Appl. Mater. Interfaces*, 2019, **11**, 35105–35114.

12 M. S. Long, P. Wang, H. H. Fang and W. D. Hu, Progress, Challenges, and Opportunities for 2D Material Based Photodetectors, *Adv. Funct. Mater.*, 2019, **29**, 1803807.

13 X. Yu, Y. Li, X. Hu, D. Zhang, Y. Tao, Z. Liu, Y. He, M. A. Haque, Z. Liu, T. Wu and Q. J. Wang, Narrow Bandgap Oxide Nanoparticles Coupled with Graphene for High Performance Mid-infrared Photodetection, *Nat. Commun.*, 2018, **9**, 4299.

14 W. X. Ouyang, F. Teng, J. H. He and X. S. Fang, Enhancing the Photoelectric Performance of Photodetectors Based on Metal Oxide Semiconductors by Charge-Carrier Engineering, *Adv. Funct. Mater.*, 2019, **29**, 1807672.

15 M. Anaya, J. P. Correa-Baena, G. Lozano, M. Saliba, P. Anguita, B. Roose, A. Abate, U. Steiner, M. Grätzel, M. E. Calvo, A. Hagfeldt and H. Míguez, Optical Analysis of $CH_3NH_3Sn_xPb_{1−x}I_3$ Absorbers: A Roadmap for Perovskite-on-perovskite Tandem Solar cells, *J. Mater. Chem. A*, 2016, **4**, 11214–11221.

16 Z. Yang, A. Rajagopal, C. C. Chueh, S. B. Jo, B. Liu, T. Zhao and A. K. Jen, Stable Low-Bandgap Pb-Sn Binary Perovskites for Tandem Solar Cells, *Adv. Mater.*, 2016, **28**, 8990–8997.

17 Y. Zhang, D. S. Jiang, J. B. Xia, L. Q. Cui, C. Y. Song, Z. Q. Zhou and W. K. Ge, A Voltage-controlled Tunable Two-color Infrared Photodetector using GaAs/AlAs/GaAlAs and GaAs/GaAlAs Stacked Multiquantum Wells, *Appl. Phys. Lett.*, 1996, **68**, 2114–2116.

18 L. Wang, J. Jie, Z. Shao, Q. Zhang, X. Zhang, Y. Wang, Z. Sun and S. T. Lee, MoS_2/Si Heterojunction with Vertically Standing Layered Structure for Ultrafast, High-Detectivity, Self-Driven Visible–Near Infrared Photodetectors, *Adv. Funct. Mater.*, 2015, **25**, 2910–2919.

19 D. Y. Guo, H. Z. Shi, Y. P. Qian, M. Lv, P. G. Li, Y. L. Su, Q. Liu, K. Chen, S. L. Wang, C. Cui, C. R. Li and W. H. Tang, Fabrication of β-Ga2O3/ZnO Heterojunction for Solar-blind Deep Ultraviolet Photodetection, *Semicond. Sci. Technol.*, 2017, **32**, 03LT01.

20 A. Hierro, G. Tabares, M. Lopez-Ponce, J. M. J. M. Ulloa, A. Kurtz, E. Muñoz, V. Marín-Borrás, V. Muñoz-Sanjosé and J.-M. Chauveau, *ZnMgO-based UV Photodiodes: a Comparison of Films Grown by Spray Pyrolysis and MBE*, San Francisco, CA, February, 2016.

21 T. Onuma, S. Saito, K. Sasaki, T. Masui, T. Yamaguchi, T. Honda and M. Higashiwaki, Valence Band Ordering in β-Ga_2O_3 Studied by Polarized Transmittance and Reflectance Spectroscopy, *Jpn. J. Appl. Phys.*, 2015, **54**, 112601.

22 Q.-M. Fu, D.-C. He, Z.-C. Yao, J.-L. Peng, H.-Y. Zhao, H. Tao, Z. Chen, Y.-F. Tu, Y. Tian, D. Zhou, G. Zheng and Z.-B. Ma, Self-powered Ultraviolet Photodetector based on ZnO Nanorod Arrays Decorated with Sea Anemone-like CuO Nanostructures, *Mater. Lett.*, 2018, **222**, 74–77.

23 D. Chen, L. Wei, L. Meng, D. Wang, Y. Chen, Y. Tian, S. Yan, L. Mei and J. Jiao, High-Performance Self-Powered UV Detector based on SnO_2-TiO_2 Nanomace Arrays, *Nanoscale Res. Lett.*, 2018, **13**, 92.

24 Y. Zhang, J. Xu, S. Shi, Y. Gao, C. Wang, X. Zhang, S. Yin and L. Li, Development of Solution-Processed ZnO Nanorod Arrays Based Photodetectors and the Improvement of UV Photoresponse via AZO Seed Layers, *ACS Appl. Mater. Interfaces*, 2016, **8**, 22647–22657.

25 Z. Xi, Z. Liu, L. Yang, K. Tang, L. Li, G. Shen, M. Zhang, S. Li, Y. Guo and W. Tang, Comprehensive Study on Ultra-Wide Band Gap La_2O_3/ϵ-Ga_2O_3 p–n Heterojunction Self-Powered Deep-UV Photodiodes for Flame Sensing, *ACS Appl. Mater. Interfaces*, 2023, **15**, 40744–40752.

26 W. Gong, J. Yan, F. Gao, S. Ding, G. He and L. Li, High-Performance UV–Vis Broad-Spectra Photodetector Based on a β-Ga_2O_3/Au/$MAPbBr_3$ Sandwich Structure, *ACS Appl. Mater. Interfaces*, 2022, **14**, 47853–47862.

27 S. K. Baek, Y. H. Kwon, J. H. Shin, H. S. Lee and H. K. Cho, Low-Temperature Processable High-Performance Electrochemically Deposited p-Type Cuprous Oxides Achieved by Incorporating a Small Amount of Antimony, *Adv. Funct. Mater.*, 2015, **25**, 5214–5221.

28 L. L. Wu, L. K. Tsui, N. Swami and G. Zangari, Photoelectrochemical Stability of Electrodeposited CuO Films, *J. Phys. Chem. C*, 2010, **114**, 11551–11556.

29 Y. Zhou and J. A. Switzer, Electrochemical Deposition and Microstructure of Copper(ı) Oxide Films, *Scr. Mater.*, 1998, **38**, 1731–1738.

30 T. Kobayashi, T. Gake, Y. Kumagai, F. Oba and Y.-I. Matsushita, Energetics and Electronic Structure of Native Point Defects in α-Ga_2O_3, *Appl. Phys. Express*, 2019, **12**, 091001.

31 P. Grez, F. Herrera, G. Riveros, A. Ramírez, R. Henríquez, E. Dalchiele and R. Schrebler, Morphological, Structural, and Photoelectrochemical Characterization of n-type CuO Thin Films Obtained by Electrodeposition, *Phys. Status Solidi A*, 2012, **209**, 2470–2475.

32 Y.-C. Chen, Y.-J. Chen, P.-H. Dong and Y.-K. Hsu, Benchmarked Photoelectrochemical Water Splitting by Nickel-Doped n-Type Cuprous Oxide, *ACS Appl. Energy Mater.*, 2020, **3**, 1373–1380.

33 Y. Wang, N. Li, P. Duan, X. Sun, B. Chu and Q. He, Properties and Photocatalytic Activity of β-Ga_2O_3 Nanorods under Simulated Solar Irradiation, *J. Nanomater.*, 2015, **2015**, 191793.

34 D. Y. Guo, Z. P. Wu, Y. H. An, P. G. Li, P. C. Wang, X. L. Chu, X. C. Guo, Y. S. Zhi, M. Lei, L. H. Li and W. H. Tang, Unipolar Resistive Switching Behavior of Amorphous Gallium Oxide Thin Films for Nonvolatile Memory Applications, *Appl. Phys. Lett.*, 2015, **106**, 042105.

35 D. Y. Guo, Z. P. Wu, Y. H. An, X. C. Guo, X. L. Chu, C. L. Sun, L. H. Li, P. G. Li and W. H. Tang, Oxygen Vacancy Tuned Ohmic-Schottky Conversion for Enhanced Performance in β-Ga_2O_3 Solar-blind Ultraviolet Photodetectors, *Appl. Phys. Lett.*, 2014, **105**, 023507.

36 Y. Liu, J. Zhu, L. Cai, Z. Yao, C. Duan, Z. Zhao, C. Zhao and W. Mai, Solution-Processed High-Quality Cu_2O Thin Films as Hole Transport Layers for Pushing the Conversion Efficiency Limit of Cu_2O/Si Heterojunction Solar Cells, *Sol. RRL*, 2019, **4**, 1900339.

37 D.-W. Jeon, H. Son, J. Hwang, A. Y. Polyakov, N. B. Smirnov, I. V. Shchemerov, A. V. Chernykh, A. I. Kochkova, S. J. Pearton and I.-H. Lee, Electrical Properties, Structural Properties, and Deep Trap Spectra of Thin α-Ga_2O_3 Films Grown by Halide Vapor Phase Epitaxy on Basal Plane Sapphire Substrates, *APL Mater.*, 2018, **6**, 121110.

38 T. Zhang, J. Lin, X. Zhang, Y. Huang, X. Xu, Y. Xue, J. Zou and C. Tang, Single-crystalline Spherical β-Ga_2O_3 Particles: Synthesis, N-doping and Photoluminescence Properties, *J. Lumin.*, 2013, **140**, 30–37.

39 X. Ren, P. Gao, X. Kong, R. Jiang, P. Yang, Y. Chen, Q. Chi and B. Li, NiO/Ni/TiO_2 Nanocables with Schottky/p-n Heterojunctions and the Improved Photocatalytic Performance in Water Splitting under Visible Light, *J. Colloid Interface Sci.*, 2018, **530**, 1–8.

40 Z. Long, X. Xu, W. Yang, M. Hu, D. V. Shtansky, D. Golberg and X. Fang, Cross-Bar SnO_2-NiO Nanofiber-Array-Based Transparent Photodetectors with High Detectivity, *Adv. Electron. Mater.*, 2019, **6**, 1901048.

41 P. Li, H. Shi, K. Chen, D. Guo, W. Cui, Y. Zhi, S. Wang, Z. Wu, Z. Chen and W. Tang, Construction of GaN/Ga_2O_3 p-n Junction for an Extremely High Responsivity Self-powered UV Photodetector, *J. Mater. Chem. C*, 2017, **5**, 10562–10570.

42 Y. Wang, C. Wu, D. Guo, P. Li, S. Wang, A. Liu, C. Li, F. Wu and W. Tang, All-Oxide NiO/Ga_2O_3 p–n Junction for Self-Powered UV Photodetector, *ACS Appl. Electron. Mater.*, 2020, **2**, 2032–2038.

43 Z. Yan, S. Li, Z. Liu, Y. Zhi, J. Dai, X. Sun, S. Sun, D. Guo, X. Wang, P. Li, Z. Wu, L. Li and W. Tang, High Sensitivity and Fast Response Self-powered Solar-blind Ultraviolet Photodetector with a β-Ga_2O_3/spiro-MeOTAD p–n Heterojunction, *J. Mater. Chem. C*, 2020, **8**, 4502–4509.

44 S. Li, Z. Yan, Z. Liu, J. Chen, Y. Zhi, D. Guo, P. Li, Z. Wu and W. Tang, A Self-powered Solar-blind Photodetector with Large Voc Eenhancing Performance Based on the PEDOT:PSS/Ga_2O_3 Organic–inorganic Heterojunction, *J. Mater. Chem. C*, 2020, **8**, 1292–1300.

45 C. Wu, F. Wu, L. Deng, S. Li, S. Wang, L. Cheng, A. Liu, J. Wang, W. Tang and D. Guo, Solution-processed Y-doped $SnSrO_3$ Electron Transport Layer for Ga_2O_3 Based Heterojunction Solar-blind Photodetector with High Sensitivity, *Vacuum*, 2022, **201**, 111064.

46 K. Arora, N. Goel, M. Kumar and M. Kumar, Ultrahigh Performance of Self-Powered β-Ga_2O_3 Thin Film Solar-Blind Photodetector Grown on Cost-Effective Si Substrate Using High-Temperature Seed Layer, *ACS Photonics*, 2018, **5**, 2391–2401.

47 L. Wu, X. Jiao, D. Wang, W. Guo, L. Li, F. Li and W. Tang, A Self-powered Deep-ultraviolet Photodetector Based on an Epitaxial Ga_2O_3/Ga:ZnO Heterojunction, *J. Mater. Chem. C*, 2017, **5**, 8688–8693.

48 J. Yu, M. Yu, Z. Wang, L. Yuan, Y. Huang, L. Zhang, Y. Zhang and R. Jia, Improved Photoresponse Performance of Self-Powered β-Ga_2O_3/NiO Heterojunction UV Photodetector by Surface Plasmonic Effect of Pt Nanoparticles, *IEEE Trans. Electron. Devices*, 2020, **67**, 3199–3204.

49 D. Guo, H. Liu, P. Li, Z. Wu, S. Wang, C. Cui, C. Li and W. Tang, Zero-Power-Consumption Solar-Blind Photodetector Based on β-Ga_2O_3/NSTO Heterojunction, *ACS Appl. Mater. Interfaces*, 2017, **9**, 1619–1628.

This journal is © The Royal Society of Chemistry 2024

J. Mater. Chem. C, 2024, **12**, 8944–8951 | **8951**